communications physics

Article

https://doi.org/10.1038/s42005-024-01715-5

Enhancing the excitation gap of a quantum-dot-based Kitaev chain

Chun-Xiao Liu ✉, A. Mert Bozkurt, Francesco Zatelli, Sebastiaan L. D. ten Haaf, Tom Dvir & Michael Wimmer

Connecting double quantum dots via a semiconductor-superconductor hybrid segment offers a platform for creating a two-site Kitaev chain that hosts Majorana zero modes at a finely tuned sweet spot. However, the effective couplings mediated by Andreev bound states in the hybrid are generally weak in the tunneling regime. As a consequence, the excitation gap is limited in size, presenting a formidable challenge for using this platform to demonstrate non-Abelian statistics and realize topological quantum computing. Here we systematically study the effects of increasing the dot-hybrid coupling. In particular, the proximity effect transforms the dot orbitals into Yu-Shiba-Rusinov states, and as the coupling strength increases, the excitation gap is significantly enhanced and sensitivity to local perturbation is reduced. We also discuss how the strong-coupling regime shows in experimentally accessible quantities, such as conductance, and provide a protocol for tuning a double-dot system into a sweet spot with a large excitation gap.

The Kitaev chain is a toy model of topological superconductivity that consists of one-dimensional spinless fermions with p-wave pairing potential[1]. In the topological phase, the endpoints host a pair of Majorana zero modes[2–13], which obey non-Abelian statistics and are regarded as the building block of topological quantum computation[14,15]. Such a Majorana qubit is predicted to be more immune to decoherence due to the quantum information being encoded nonlocally in space and further protected by an excitation gap above the computational subspace.

In solid-state physics, the Kitaev chain model can be simulated in a quantum dot array by utilizing the spin-polarized dot orbitals as spinless fermions, with the effective couplings mediated by superconductivity[16]. Remarkably, even a chain consisting of only two quantum dots can exhibit fine-tuned, but still spatially separated Majorana modes at a sweet spot, colloquially called poor man's Majorana modes[17]. Recently, such a two-site Kitaev chain was experimentally realized in double quantum dots, and poor man's Majorana modes were identified via conductance spectroscopy at the sweet spot[18]. In particular, the effective couplings, both normal and superconducting ones, are mediated by an Andreev bound state (ABS) in a hybrid segment connecting both quantum dots[19], which allows for a deterministic fine-tuning of the relative amplitude by changing the ABS chemical potential via electrostatic gating[20–22]. This effect was shown theoretically to be robust to Coulomb interactions in the dots as well as stronger coupling[23].

Despite the experimental progress, state-of-the-art Kitaev chain devices are still constrained by a relatively small excitation gap (~25 μeV), which is much smaller than the induced gap of the ABS (~150 μeV) and the parent aluminum gap (~230 μeV)[18]. In order to experimentally demonstrate the non-Abelian statistics of Majoranas and to obtain high-quality Majorana qubits[24–26], a significant enhancement in the excitation gap is crucial. This enhancement will allow for a more tolerant adiabatic limit condition $\sim \hbar/E_{\mathrm{gap}}^{-1}$ [27–30] and suppress the detrimental thermal effects $\sim e^{-E_{\mathrm{gap}}/k_B T}$ [31].

In this work, we use the three-site model[19,23,32] to systematically study enhancing the energy gap by increasing the dot-hybrid coupling strength, achievable in experiments by lowering the tunnel barrier height. As a result of the proximity effect from the hybrid, the spin-polarized orbitals in the quantum dots undergo a transformation into Yu–Shiba–Rusinov (YSR) states[33,34], in an analogy with the conventional YSR states[35–37]. These states then constitute the new spinless fermion basis for the emulated Kitaev chain. Thus, the concepts of elastic cotunneling and crossed Andreev reflection in the weak coupling regime have to be generalized. Most importantly, we show that poor man's Majorana zero modes can survive in this strong coupling regime, featuring a significantly enhanced excitation gap. The properties of the resulting states are different from those in the weak coupling regime, showing both wavefunction profiles and conductance properties while maintaining their Majorana character.

Methods

Model and Hamiltonian

A two-site Kitaev chain device consists of two separated quantum dots connected by a hybrid segment [see Fig. 1a]. The system Hamiltonian

QuTech and Kavli Institute of Nanoscience, Delft University of Technology, Delft 2600 GA, The Netherlands. ✉e-mail: chunxiaoliu62@gmail.com

is[19,23,32]

$$
\begin{aligned}
H &= H_D + H_S + H_T,\\
H_D &= \sum_{a=L,R} (\varepsilon_{Da} + E_{ZDa}) n_{Da\uparrow} + (\varepsilon_{Da} - E_{ZDa}) n_{Da\downarrow}\\
&\quad + U_{Da} n_{Da\uparrow} n_{Da\downarrow},\\
H_S &= \varepsilon_A (n_{A\uparrow} + n_{A\downarrow}) + \Delta_0 (c_{A\uparrow} c_{A\downarrow} + c^\dagger_{A\downarrow} c^\dagger_{A\uparrow}),\\
H_T &= \sum_{\sigma=\uparrow,\downarrow} \Big(t_L c^\dagger_{A\sigma} c_{DL\sigma} + \sigma t_{Lso} c^\dagger_{A\bar{\sigma}} c_{DL\sigma}\\
&\quad + t_R c^\dagger_{DR\sigma} c_{A\sigma} + \sigma t_{Rso} c^\dagger_{DR\bar{\sigma}} c_{A\sigma} \Big) + h.c.,
\end{aligned}
\tag{1}
$$

where H_D is the Hamiltonian of the quantum dots, $n_{Da\sigma} = c^\dagger_{Da\sigma} c_{Da\sigma}$ is the electron occupancy number on dot a, ε_{Da} is the orbital energy, E_{ZDa} is the strength of the induced Zeeman energy, and U_{Da} is the Coulomb repulsion strength. H_S describes the hybrid segment hosting a pair of ABSs in the low-energy approximation. ε_A is the normal-state energy, and Δ_0 is the induced pairing gap. While we assume no induced Zeeman energy in the ABS due to a strong renormalization effect at the hybrid interface[38,39], the main conclusions remain valid for finite Zeeman energy as well. H_T is the tunnel coupling between dot and ABS, including both spin-conserving $\sim t$ and spin-flipping $\sim t_{so}$ processes. In realistic devices, the amplitude of t is a variable that can be controlled by tunnel barrier gates, while the ratio of t_{so}/t is generally fixed and is determined by the strength of spin-orbit interaction. In the rest of this work, we will choose Δ_0 to be the natural unit. Unless stated otherwise, we set $E_{ZDa} = 1.5\,\Delta_0$, $U_{Da} = 5\,\Delta_0$, and $t_{aso}/t_a = 0.3$ according to the recent experimental measurements on similar devices[18,20–22]. In addition, we numerically calculate the differential conductance using the rate-equation method[23], where the lead tunneling rate is $\Gamma_a = 0.025\Delta_0$, and temperature is $k_B T = 0.02\,\Delta_0$.

Results

Quantum dot-Andreev bound state pair

To assess the strength and to understand the effects of dot-hybrid coupling, we first focus on the conductance spectroscopy of a single quantum dot-ABS pair. Hence, for the discussions here, we temporarily remove the right dot in the model Hamiltonian in Eq. (1). Figure 2 shows the zero-bias conductance spectroscopy in the $(\varepsilon_D, \varepsilon_A)$ plane for $t/\Delta_0 = 0.25$, 1 and 2, respectively. Here $G_{LL} = dI_L/dV_L$ at $V_L = 0$. As shown in Fig. 2a, in the weak coupling regime, the conductance resonances are two straight lines extending along ε_A, corresponding to the spin-up and down orbitals in the quantum dot. In contrast, with a strong dot-hybrid coupling, the resonance lines become *S*-shaped curves [see Fig. 2b], and the conductance magnitudes are increased by order of magnitude. For even stronger coupling, Fig. 2c, proximity from the ABS is so strong that the states are very different from spin-up and spin-down, as signified by the differently connected arcs in the conductance.

This qualitative behavior was already described in existing literature[34]. Here, we recover the same behavior in a simpler model and also consider the magnitude of the conductance. In particular, we can use second-order perturbation theory to qualitatively understand the physical mechanisms underlying these conductance features.

First, the dot-hybrid coupling renormalizes the dot orbital energy by $\delta\varepsilon_D$ via cotunneling processes. Up to the leading order of t and t_{so}, this energy renormalization is

$$
\delta\varepsilon_D = \left(t^2 + t_{so}^2\right) \frac{u^2 - v^2}{E_A} + O\left(t^4, t_{so}^4\right), \tag{2}
$$

where $u^2 = 1 - v^2 = 1/2 + \varepsilon_A/2E_A$ are the BCS coherence factors and $E_A = \sqrt{\varepsilon_A^2 + \Delta_0^2}$ is the ABS excitation energy. Interestingly, due to destructive interference, the dot energy shifts positively (negatively) for $\varepsilon_A > 0$ ($\varepsilon_A < 0$), vanishes at $\varepsilon_A = 0$, and decays as ε_A^{-1} for large ε_A, well explaining the *S*-shaped conductance resonances shown in Fig. 2b. Hence, the *S*-shaped feature is a clear sign of the proximity effect due to the ABS in the hybrid semiconductor–superconductor segment (rather than directly to the parent metallic superconductor), and the increase in bending is a direct signal of increasing coupling.

From Fig. 2a, b, we also observe that conductance is largest when the ABS is near resonance, i.e., $-\Delta_0 < \varepsilon_A < \Delta_0$, which can also be understood from perturbation theory. The ABS will induce a pairing term on the quantum dot, i.e., $\Delta_{\text{ind}} c^\dagger_{D\uparrow} c^\dagger_{D\downarrow} + h.c.$ via local Andreev reflection with

$$
\Delta_{\text{ind}} = \left(t^2 + t_{so}^2\right) \frac{2uv}{E_A} + O\left(t^4, t_{so}^4\right). \tag{3}
$$

The induced gap size is prominent within $-\Delta_0 < \varepsilon_A < \Delta_0$ and decays as ε_A^{-2} outside. As a result, the local Andreev conductance is significantly enhanced when ABS is near resonance and vanishes when off-resonance. Thus, based on the shape of the resonance lines as well as on the enhancement of the Andreev conductance, one can estimate the strength of the dot-hybrid coupling in an actual device. In addition, although not the main focus of the current work, it is likely that the continuum states of the parent superconductor also induce local proximity effect on the quantum

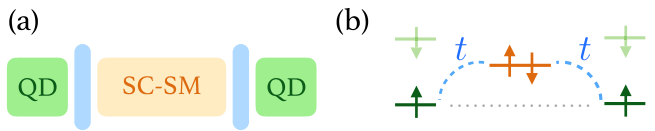

Fig. 1 | Device schematic. a Schematic of a two-site Kitaev chain device. Two separated quantum dots (green) are connected by a hybrid segment (orange) in the middle, with the strength of the dot-hybrid coupling being controlled by the tunnel gates (blue). **b** Schematic of the dot orbitals and Andreev bound states introduced in the model Hamiltonian. The blue dashed lines and t denote the dot-hybrid tunneling, and the gray dotted line represents the superconducting Fermi energy.

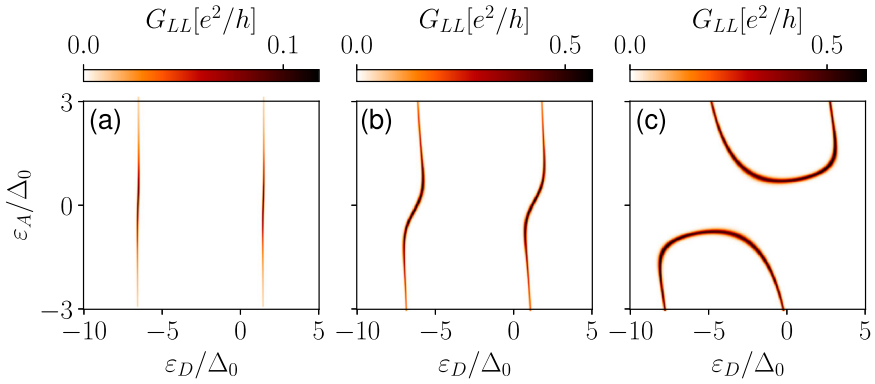

Fig. 2 | Local conductance spectroscopy for a dot-Andreev bound state pair. The local zero-bias conductance on the quantum dot-Andreev bound state pairs G_{LL} with different values for the tunneling strength. $t/\Delta_0 = 0.25$, 1, 2 in panels (**a**–**c**), respectively.

dot. Such contribution would be a constant that is independent of the ABS chemical potential, i.e., $\Delta_{\rm ind} \to \Delta_{\rm ind} + \Delta_{\rm ind}^{\rm qp}$. More importantly, especially in the strong coupling regime, the induced superconducting effect would transform the dot orbitals into YSR states[34,40–46]. These states then establish the new spinless fermion basis for the emulated Kitaev chain.

Coupled YSR states

We now turn to the case of two quantum dots coupled via an ABS and develop an effective theory for two coupled YSR states. By assuming that the ABS in the hybrid remains gapped, we can integrate it and obtain the effective coupling

$$H^{\rm eff}_{\rm coupling} = \sum_{\sigma,\eta=\uparrow,\downarrow} \left(t_{\sigma\eta} c^\dagger_{DL\sigma} c_{DR\eta} + \Delta_{\sigma\eta} c^\dagger_{DL\sigma} c^\dagger_{DR\eta} \right) + h.c., \tag{4}$$

where $t_{\sigma\eta}$ and $\Delta_{\sigma\eta}$ are the elastic cotunneling (ECT) and crossed Andreev reflection (CAR) amplitudes between electron or hole excitations in the two dots. These couplings are tunable by changing the energy of the middle dot, ε_A[19]. Note that the problem of coupling two quantum dots via ECT and CAR, and in the presence of local Andreev reflection giving rise to a proximity effect in the dots has been studied extensively before[47–50], predominantly at zero magnetic field. In contrast, we focus on the case of a significant Zeeman splitting in the outer quantum dots, such that the ground state of both dots occupied by a single electron is a triplet state. We also emphasize that the treatment in Eq. (4) is valid when the dot-ABS coupling is weak ($t \ll \Delta_0$) or intermediate in strength ($t \lesssim \Delta_0$), while the quantum dot orbitals can be strongly proximitized by the ABS or the continuum states in the parent superconductor.

For unproximitized quantum dots, Eq. (4) plus H_D in Eq. (1) indeed resembles the Hamiltonian of a two-site Kitaev chain[1]. However, since YSR states are a superposition of electron and hole components, the effective couplings of ECT and CAR have to be generalized. In particular, for a single proximitized quantum dot with finite Zeeman splitting, the ground states in the even- and odd-parity subspaces are a spin singlet and a spin-down state, respectively,

$$|S\rangle = u|00\rangle - v|11\rangle, \quad |\downarrow\rangle = |01\rangle \tag{5}$$

where $u^2 = 1 - v^2 = 1/2 + \xi/2E_0$ are the BCS coherence factors, with $\xi = \varepsilon + U/2$ and $E_0 = \sqrt{\xi^2 + \Delta^2_{\rm ind}}$, and $|n_\uparrow n_\downarrow\rangle$ is a state in the occupancy representation. Consequently, we define YSR state as $|\downarrow\rangle = f^\dagger_{\rm YSR}|S\rangle$, with an excitation energy $\delta\varepsilon = E_\downarrow - E_S$. When coupling two YSR states via the ABS, the effective Hamiltonian becomes

$$H_{\rm eff} = \sum_{a=L,R} \delta\varepsilon_a f^\dagger_a f_a + \Gamma_o f^\dagger_L f_R + \Gamma_e f^\dagger_L f^\dagger_R + h.c., \tag{6}$$

where f_a denotes the YSR state in dot-a, with $\delta\varepsilon_a$ being the excitation energy. This also takes the form of a Kitaev Hamiltonian, but now in the basis of YSR states. Crucially, $\Gamma_{o/e}$ represents the generalized effective couplings between YSR states. The odd-parity coupling is

$$\begin{aligned} \Gamma_o &= \langle S\downarrow | H^{\rm eff}_{\rm coupling} | \downarrow S\rangle, \\ &= -t_{\uparrow\uparrow} v_L v_R + t_{\downarrow\downarrow} u_L u_R + \Delta_{\uparrow\downarrow} v_L u_R - \Delta_{\downarrow\uparrow} u_L v_R, \end{aligned} \tag{7}$$

where $|\downarrow S\rangle, |S\downarrow\rangle$ are the tensor states with total parity odd, and u_a, v_a are the BCS factors defined in Eq. (5). Note that Γ_o is a linear combination of equal-spin ECT and opposite-spin CAR, which are all spin-conserving processes. On the other hand, the even-parity coupling is

$$\begin{aligned} \Gamma_e &= \langle SS | H^{\rm eff}_{\rm coupling} | \downarrow\downarrow\rangle, \\ &= -\Delta_{\uparrow\uparrow} v_L v_R + \Delta_{\downarrow\downarrow} u_L u_R + t_{\uparrow\downarrow} v_L u_R - t_{\downarrow\uparrow} u_L v_R, \end{aligned} \tag{8}$$

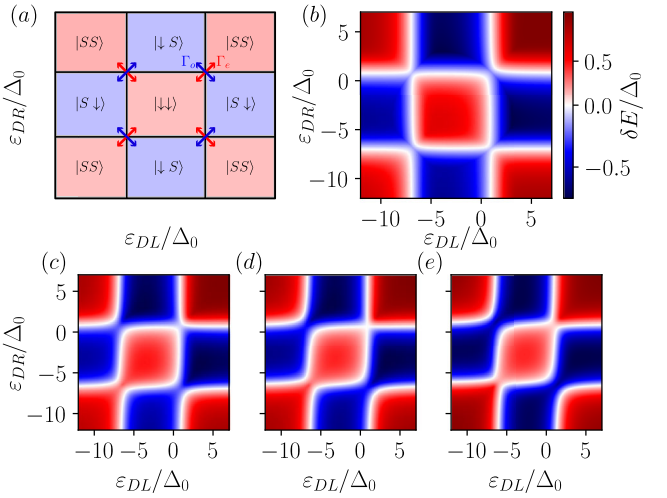

Fig. 3 | The charge stability diagram and the coupling processes. a Schematic description of the charge stability diagram. Γ_e (red arrows) and Γ_o (blue arrows) couples even and odd states, respectively. **b** Charge stability diagram with $t_{so} = 0$ and $\varepsilon_A = -1.5\Delta_0$. In this case, only spin-conserving processes are allowed, resulting in a ring-like pattern in the charge stability diagram. Charge stability diagrams for different values of ε_A. In particular, for orbital energies $\varepsilon_{DL} \approx \varepsilon_{DR} \approx 0$, in **c** Γ_o dominates with $\varepsilon_A = \varepsilon^*_A - 0.2\Delta_0$, in **d** it shows the sweet spot $\varepsilon_A = \varepsilon^*_A$, and in **e** Γ_e dominates $\varepsilon_A = \varepsilon^*_A + 0.2\Delta_0$. Here $\varepsilon^*_A \approx -0.269\Delta_0$ is the sweet spot value. In panels **b**–**e**, we use $t = \Delta_0$. Panels **b**–**e** share the same colorbar.

which couples states with total spin zero and one. In particular, a finite Γ_e requires a physical mechanism to break spin conservation, e.g., spin-orbit interaction.

Figure 3a shows a schematic of the charge stability diagram as a function of the quantum dot energies. Blue and red squares indicate whether the ground state of two uncoupled dots is odd or even, respectively. Note that the singlet ground state in the dots does depend on the dot energies through the values of u_a and v_a. For example, in the upper-right corner $u_{L/R} > v_{L/R}$, corresponding to each dot predominantly empty, whereas the lower-left corner features $u_{L/R} < v_{L/R}$, corresponding to each dot predominantly doubly occupied. The arrows represent the interactions $\Gamma_{o/e}$, and the relative strength of these couplings will determine the ground state close to the four corners in the charge stability diagram where each dot exhibits a degeneracy without interactions. Additionally, we point out the role of CAR and ECT interchange for different corners of the charge stability diagram.

In the absence of spin–orbit interaction, $\Gamma_e = 0$, and in general $\Gamma_o \neq 0$. Hence, at the four corners, the energy of the odd ground state is lowered compared to the even ones. This can also be observed in a simulation of the full three-dot Hamiltonian in Eq. (1), as shown in Fig. 3b, where we find a disconnected even island in the center of the charge stability diagram. Note that such behavior is only possible for a finite Zeeman splitting and, as such, qualitatively different from the charge stability diagrams[49].

For a system with finite spin–orbit coupling, in general, also $\Gamma_e \neq 0$, and the respective values will depend on details of the system (such as the energy ε_A of the middle dot that can be used to tune ECT and CAR). In particular, it is now, in general, possible to change the relative strength of $\Gamma_{e/o}$. This shows as a change in connectivity in the charge stability diagram, with a guaranteed sweet spot $\Gamma_e = \Gamma_o$ in between. We show this behavior in Fig. 3c–e on the example of the upper-right corner as we vary ε_a, transitioning from a regime dominated by Γ_o in Fig. 3c to one dominated by Γ_e in Fig. 3e. When $\Gamma_e = \Gamma_o$, a cross emerges in the phase diagram as a signature of the sweet spot, as shown in Fig. 3d.

In the limit of large Coulomb interaction U on the outer dots, either $u_{L/R} \approx 1$ or $v_{L/R} \approx 1$ and $\Gamma_{e/o}$ will be dominated by a single ECT or CAR term, as evident from Eqs. (7) and (8).

More generally, however, in the limit of vanishing Zeeman splitting in the middle dot, CAR and ECT coupling are constrained by $t_{\uparrow\uparrow} = t_{\downarrow\downarrow}, t_{\uparrow\downarrow} = -t_{\downarrow\uparrow}, \Delta_{\uparrow\uparrow} = \Delta_{\downarrow\downarrow}, \Delta_{\uparrow\downarrow} = -\Delta_{\downarrow\uparrow}$, due to time-reversal symmetry, such that $\Gamma_{o/e}$ can be further simplified as

$$\begin{aligned}\Gamma_o &= t_{\uparrow\uparrow}\cos(\beta_L+\beta_R) + \Delta_{\uparrow\downarrow}\sin(\beta_L+\beta_R),\\ \Gamma_e &= \Delta_{\uparrow\uparrow}\cos(\beta_L+\beta_R) + t_{\uparrow\downarrow}\sin(\beta_L+\beta_R),\end{aligned} \tag{9}$$

where $0 \le \beta_a \le \pi/2$ is a parameter to characterize the BCS factors by $u_a = \cos\beta_a, v_a = \sin\beta_a$. For two dots with a similar level of proximity effect, the diagonal corners in Fig. 3 will have $\beta_L = \beta + \delta/2, \beta_R = \beta - \delta/2$, with $\delta \ll 1$ characterizing a weak asymmetry. As a result, the odd- and even-parity couplings reduce to

$$\begin{aligned}\Gamma_o &\approx t_{\uparrow\uparrow}\cos(2\beta) + \Delta_{\uparrow\downarrow}\sin(2\beta),\\ \Gamma_e &\approx \Delta_{\uparrow\uparrow}\cos(2\beta) + t_{\uparrow\downarrow}\sin(2\beta).\end{aligned} \tag{10}$$

This indicates that as the proximity effect increases, the initially purely equal-spin ECT/CAR coupling ratio Γ_o/Γ_e gains a finite opposite-spin CAR/ECT component. In contrast, around the off-diagonal corners, we have $\beta_L = \beta + \delta/2, \pi/2 - \beta_R = \beta - \delta/2$, yielding

$$\begin{aligned}\Gamma_o &\approx \Delta_{\uparrow\downarrow}\cos(\delta) - t_{\uparrow\uparrow}\sin(\delta),\\ \Gamma_e &\approx t_{\uparrow\downarrow}\cos(\delta) - \Delta_{\uparrow\uparrow}\sin(\delta).\end{aligned} \tag{11}$$

Interestingly, despite the proximity effect, $\Gamma_{o/e}$ is equal to the only ECT or CAR just as in the unproximitized regime. Only an asymmetry in the proximity effect leads to a mixing of CAR and ECT-type couplings. For a detailed investigation of how Γ_e and Γ_o behave in different corners of the charge stability diagram, we refer to Supplementary Note 1: Γ_e and Γ_o for different corners of the charge stability diagram.

Poor man's Majorana

We now focus on the properties of the poor man's Majoranas that appear at the sweet spot in the full dot-hybrid-dot system. Without loss of generality, we assume that the left and right dots have the same set of physical parameters, e.g., $\varepsilon_{DL} = \varepsilon_{DR} = \varepsilon_D, E_{ZL} = E_{ZR} = 1.5\Delta_0, U_L = U_R = 5\Delta_0, t_L = t_R = t$ and $t_{Lso} = t_{Rso} = 0.3t$. To simplify, we introduce a shift in dot energy $\varepsilon_D \to \varepsilon_D - E_{ZD}$ to set the zero energy of the spin-down orbital at $\varepsilon_D = 0$. Figure 4a shows the phase diagram in the $(\varepsilon_A, \varepsilon_D)$ plane for weakly coupled quantum dots ($t/\Delta_0 = 0.25$), with $\delta E = E_{\rm gs}^{\rm odd} - E_{\rm gs}^{\rm even}$ being the energy difference of the ground states in the opposite fermion parity subspace. The white-colored curves ($\delta E = 0$) represent the ground state degeneracy, with the tip of the curves (marked by a black cross sign) indicating the sweet spot[23]. At this sweet spot, the effective normal and superconducting couplings of the two dots become equal in strength. The wavefunction profiles plotted in Fig. 4b further demonstrate that the Majorana zero modes are well localized at the two dots, respectively, with only a negligible amount of overlap in the middle ABS. Here, the Majorana wavefunction densities are defined for site and spin

$$\begin{aligned}\rho_{1a\sigma} &= |\langle o|(c_{a\sigma} + c_{a\sigma}^\dagger)|e\rangle|^2,\\ \rho_{2a\sigma} &= |\langle o|(c_{a\sigma} - c_{a\sigma}^\dagger)|e\rangle|^2,\end{aligned} \tag{12}$$

where $a = L, M, R, \sigma = \uparrow, \downarrow$, and $|e\rangle, |o\rangle$ denote the even- and odd-parity ground state.

Comparatively, the lower panels in Fig. 4 show the results obtained in the strong dot-ABS coupling regime with $t/\Delta_0 = 1$. Around the sweet spot marked by the black cross sign, the ground state degeneracy line now becomes much broader and straighter compared to the weak coupling regime, indicating a significantly enhanced energy gap and robustness against dot chemical potential fluctuations. In Fig. 4d, the plotted Majorana wavefunctions show strong leakage into the middle ABS and small leakage to the opposite normal dot with opposite spin. We emphasize that the wavefunction overlap in the ABS, which is a virtual state, is not detrimental,

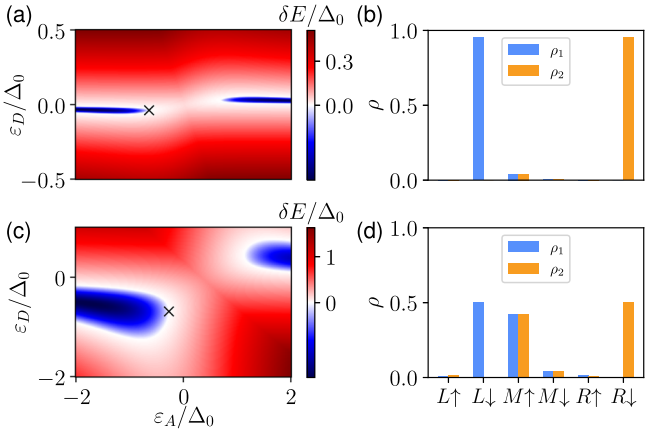

Fig. 4 | Features of weak vs. strong coupling regimes. a Phase diagram and **b** Majorana wavefunction profiles in the weak dot-ABS coupling regime ($t/\Delta_0 = 0.25$). In panels **c** and **d**, we show the same physical quantities calculated in the strong coupling regime ($t/\Delta_0 = 1$). The black crosses in panels **a** and **c** represent the sweet spot parameters for weak and strong coupling regimes, respectively. In panels **b** and **d**, the bars in blue and orange denote two Majoranas profiles defined in Eq. (12).

and that the reduced density on the normal dots will only reduce the visibility of the Majorana from the external detecting system.

To gain a better understanding of the effect of strong coupling, we now investigate the continuous evolution of the sweet spot and the properties of Majoranas as a function of t. To that end, we define the following quantities: excitation gap ($E_{\rm gap}$), Majorana localization (ρ), and polarization (χ)[23] as below

$$\begin{aligned}E_{\rm gap} &= \min(\delta E_{oe}^1, \delta E_{eo}^1),\\ \rho &= \rho_{1L} = \rho_{1L\uparrow} + \rho_{1L\downarrow},\\ \chi &= (\rho_{1L} - \rho_{2L})/(\rho_{1L} + \rho_{2L}).\end{aligned} \tag{13}$$

Here, $E_{\rm gap}$ represents the excitation gap above the poor man's Majorana zero modes, where δE_{oe}^1 and δE_{eo}^1 denote the energy differences between the ground state in one parity sector and the first excited state in the opposite one. The Majorana localization ρ and Majorana polarization χ, both of which are defined on the outer quantum dot, characterize the localization and overlap of the Majorana wavefunction on the normal dot, respectively.

Figure 5a shows the evolution of the positions of the sweet spots in the $(\varepsilon_A, \varepsilon_D)$ plane. As the coupling strength t increases, the effect of dot energy renormalization predicted by Eq. (2) becomes more pronounced, making ε_D deviate from the value of $\varepsilon_D = 0$ in the weak coupling regime. At the same time, the sweet-spot values of ε_A shift towards a more positive value, indicating an induced Zeeman energy in ABS[19], which comes from the inverse proximity effect from the quantum dot. One crucial aspect of the strong coupling regime is that, with increasing t, the excitation gap is enhanced significantly in a nearly quadratic manner [see Fig. 5b]. The excitation gap reaches as high as $E_{\rm gap} \sim 0.7\Delta_0$ for a dot-hybrid coupling $t/\Delta_0 = 1.1$. Moreover, we observe that the degree of protection against detuning of both quantum dots away from the sweet spot increases with the growing t, as evidenced by the diminishing curvature of the quadratic splitting of ground state degeneracy in Fig. 5c. On the other hand, the Majorana localization ρ is largely reduced due to increased wavefunction leakage into the middle ABS when the tunnel barrier is lowered. Yet, although the middle dot hybridizes strongly with the Majoranas in the outer dots, the Majorana polarization χ decreases much slower. Hence, even for strong coupling, the overlap of Majoranas on the outer dots remains small, which will be beneficial for future qubit experiments.

We observe these changes manifesting in the local conductance profile calculated at the sweet spot [see Fig. 5d]. Specifically, as t increases, the

height of the Majorana-induced zero-bias conductance peaks decreases due to the reduction in Majorana density at the outer dot, which in turn reduces its effective coupling strength with the normal lead. In addition, the voltage bias values where the side peaks appear, indicating the magnitude of the excitation gap, increases with t, and a single side peak begins to split into two at larger t values, consistent with our findings in Fig. 5b.

Signatures of strong coupling in nonlocal transport

Nonlocal transport is a useful tool for probing hybrid systems, as the nonlocal conductances G_{LR} and G_{RL} can measure the BCS charge of states[51] in non-interacting systems. For example, in a recent experiment, nonlocal conductance was used to confirm the chargeless Majorana character of the zero-energy state[18].

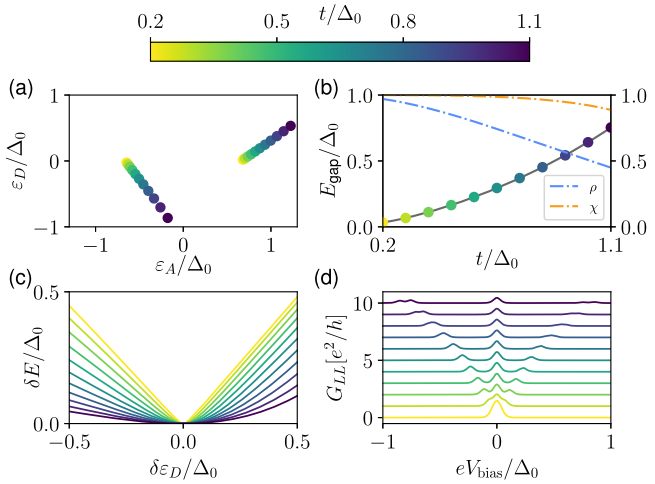

Fig. 5 | The evolution of the relevant quantities of poor man's Majorana as a function of the coupling strength t. a The evolution of the position of the sweet spot in the phase diagram as a function of t. In **b**, we depict the evolution of the excitation gap at the sweet spot and the Majorana density ρ and polarization χ on the left quantum dot. **c** depicts the ground state degeneracy splitting when both quantum dots chemical potentials are detuned away from the sweet spot. As t increases, the amount of splitting diminishes. **d** Waterfall plots of local conductance profile at the sweet spot for each t. Even though the main peak height decreases as t increases, the side peaks that signify the excitation gap appear at a larger bias and, furthermore, split.

We now discuss how the visibility of the first excited state in the nonlocal conductance G_{LR} is a qualitative indicator of the strong coupling regime. In Fig. 6, we show the nonlocal conductances in both weak coupling ($t = 0.25\,\Delta_0$) and strong coupling ($t = \Delta_0$) regimes, as a function of the applied voltage bias V_{bias} and chemical potential detuning away from the sweet spot $\delta\varepsilon_{DR}$. In the weak coupling regime, shown in Fig. 6a, b, the conductance signal strength for G_{LR} is significantly lower than its counterpart G_{RL}. This behavior is in line with the results for a spinless Kitaev chain model[18]. There, the chargeless nature of the excited state leads to a vanishing G_{LR} signal. In contrast, as we increase the dot-hybrid coupling, this effective picture breaks down, and the nonlocal conductances G_{LR} and G_{RL} become comparable in strength, as demonstrated in Fig. 6c, d. Furthermore, G_{RL} for the first excited state changes sign as a function of detuning $\delta\varepsilon_{DR}$ in the right dot, whereas G_{LR} does not. The calculations of a complete conductance matrix, including both local and nonlocal conductances, can be found in Supplementary Note 2: Conductance matrix for weak and strong coupling regimes.

In Fig. 6e, we track the evolution of maximum nonlocal conductance signal strength with varying t. We observe that the maximum conductance for G_{LR} increases much faster with increasing t compared to G_{RL}. We can attribute the increase in G_{LR} to the increase in the BCS charge of the excited state in the left quantum dot with increasing t, as shown in Fig. 6f[51].

Discussion

In this work, we have studied a dot-hybrid-dot system in the strong dot-hybrid coupling regime ($t \sim \Delta_0$) for implementing a two-site Kitaev chain. Due to the proximity effect from the ABS, the dot orbitals undergo a transformation into YSR states, which constitute the new spinless fermion basis for the effective Kitaev chain, and we have studied their coupling as mediated by the middle dot. Importantly, poor man's Majorana zero modes persist in this strong coupling regime and now possess a significantly enhanced excitation gap. On the other hand, there is an upper bound for the dot-hybrid coupling strength. As shown in Fig. 2c, an excessively strong coupling $t \sim 2E_{ZD}$ leads to the hybridization of dot orbitals with opposing spins, gapping out the zero-energy YSR states. That is, a sufficiently strong Zeeman field ($E_{ZD} \gg t$) is always a prerequisite for obtaining an effectively spinless Kitaev chain model in a spinful physical system[52,53].

Additionally, our theoretical work provides a practical recipe for implementing a two-site Kitaev chain with an enhanced excitation gap. Specifically, one can reach the desirable dot-hybrid coupling regime by observing the conductance spectroscopy of a single quantum dot-ABS while shifting the other dot off-resonance, e.g., Fig. 2b. Performing this procedure

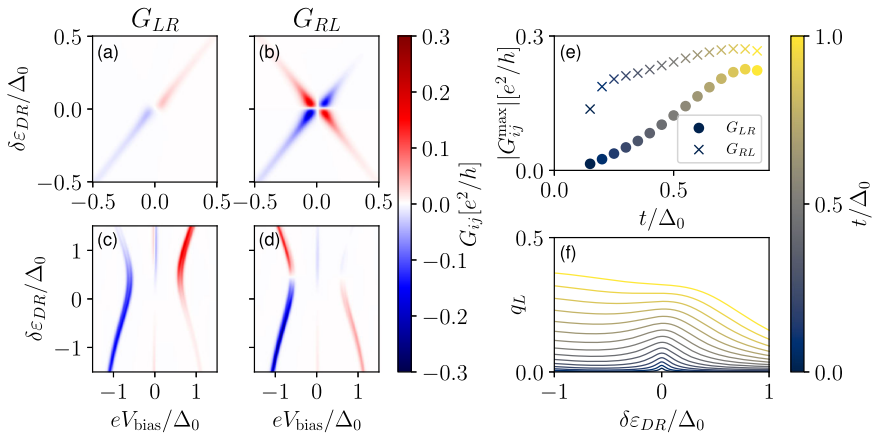

Fig. 6 | Conductance features in weak and strong coupling regimes. Nonlocal conductances in **a**, **b** the weak coupling ($t = 0.25\Delta_0$) and **c**, **d** strong coupling regimes ($t = \Delta_0$): In both scenarios, we detune the right quantum dot chemical potential from the sweet spot by $\delta\varepsilon_{DR}$. In the strong coupling regime, we observe an increased gap, while the maximum conductance signal for G_{LR} strengthens, whereas G_{RL} remains relatively stable. Panel **e** illustrates how the maximum conductance signal strength evolves with varying t, indicated by the color of the circles. As we increase the quantum dot-hybrid coupling t, G_{LR} (circles) shows significant enhancement, while G_{RL} (crosses) remains mostly constant. This increase in G_{LR} is attributed to the increased BCS charge of the excited state in the left quantum dot, shown in panel (**f**), with increasing t, leading to an increased conductance signal magnitude.

for both left and right pairs, the sweet spot can be further fine-tuned by changing the chemical potential of the ABS to find a crossing in the charge stability diagram [see Fig. 3c–e] and a robust zero-bias peak in the conductance spectroscopy [see Fig. 5d]. Indeed, a parallel experimental work[54] has achieved an energy gap of approximately ~75 μeV using the aforementioned procedure, verifying the theoretical predictions proposed in this work. We thus expect that our work provides useful guidelines and insights for realizing Kitaev chains in the strong coupling regime, serving as the central platform for future research on Majorana quasiparticles and non-Abelian statistics.

Data availability

The data that support the findings of this study have been deposited in Zenodo[55].

Code availability

The code used to generate the figures is available on Zenodo[55].

Received: 17 January 2024; Accepted: 24 June 2024;
Published online: 13 July 2024

References

1. Kitaev, A. Y. Unpaired Majorana fermions in quantum wires. *Physics* **44**, 131 (2001).
2. Alicea, J. New directions in the pursuit of Majorana fermions in solid state systems. *Rep. Prog. Phys.* **75**, 076501 (2012).
3. Leijnse, M. & Flensberg, K. Introduction to topological superconductivity and Majorana fermions. *Semicond. Sci. Technol.* **27**, 124003 (2012).
4. Beenakker, C. Search for Majorana fermions in superconductors. *Annu. Rev. Condens. Matter Phys.* **4**, 113–136 (2013).
5. Stanescu, T. D. & Tewari, S. Majorana fermions in semiconductor nanowires: fundamentals, modeling, and experiment. *J. Phys.* **25**, 233201 (2013).
6. Jiang, J.-H. & Wu, S. Non-Abelian topological superconductors from topological semimetals and related systems under the superconducting proximity effect. *J. Phys.* **25**, 055701 (2013).
7. Elliott, S. R. & Franz, M. Colloquium: Majorana fermions in nuclear, particle, and solid-state physics. *Rev. Mod. Phys.* **87**, 137–163 (2015).
8. Sato, M. & Fujimoto, S. Majorana fermions and topology in superconductors. *J. Phys. Soc. Jpn* **85**, 072001 (2016).
9. Sato, M. & Ando, Y. Topological superconductors: a review. *Rep. Prog. Phys.* **80**, 076501 (2017).
10. Aguado, R. Majorana quasiparticles in condensed matter. *La Riv. Nuovo Cim.* **40**, 523–593 (2017).
11. Lutchyn, R. M. et al. Majorana zero modes in superconductor–semiconductor heterostructures. *Nat. Rev. Mater.* **3**, 52–68 (2018).
12. Zhang, H., Liu, D. E., Wimmer, M. & Kouwenhoven, L. P. Next steps of quantum transport in Majorana nanowire devices. *Nat. Commun.* **10**, 5128 (2019).
13. Frolov, S. M., Manfra, M. J. & Sau, J. D. Topological superconductivity in hybrid devices. *Nat. Phys.* **16**, 718–724 (2020).
14. Nayak, C., Simon, S. H., Stern, A., Freedman, M. & Das Sarma, S. Non-Abelian anyons and topological quantum computation. *Rev. Mod. Phys.* **80**, 1083–1159 (2008).
15. Sarma, S. D., Freedman, M. & Nayak, C. Majorana zero modes and topological quantum computation. *Npj Quantum Inf.* **1**, 15001 EP – (2015).
16. Sau, J. D. & Sarma, S. D. Realizing a robust practical Majorana chain in a quantum-dot-superconductor linear array. *Nat. Commun.* **3**, 964 (2012).
17. Leijnse, M. & Flensberg, K. Parity qubits and poor man's Majorana bound states in double quantum dots. *Phys. Rev. B* **86**, 134528 (2012).
18. Dvir, T. et al. Realization of a minimal Kitaev chain in coupled quantum dots. *Nature* **614**, 445–450 (2023).
19. Liu, C.-X., Wang, G., Dvir, T. & Wimmer, M. Tunable superconducting coupling of quantum dots via Andreev bound states in semiconductor-superconductor nanowires. *Phys. Rev. Lett.* **129**, 267701 (2022).
20. Wang, G. et al. Singlet and triplet cooper pair splitting in hybrid superconducting nanowires. *Nature* **612**, 448–453 (2022).
21. Wang, Q. et al. Triplet correlations in cooper pair splitters realized in a two-dimensional electron gas. *Nat. Commun.* **14**, 4876 (2023).
22. Bordin, A. et al. Tunable crossed Andreev reflection and elastic cotunneling in hybrid nanowires. *Phys. Rev. X* **13**, 031031 (2023).
23. Tsintzis, A., Souto, R. S. & Leijnse, M. Creating and detecting poor man's Majorana bound states in interacting quantum dots. *Phys. Rev. B* **106**, L201404 (2022).
24. Liu, C.-X., Pan, H., Setiawan, F., Wimmer, M. & Sau, J. D. Fusion protocol for Majorana modes in coupled quantum dots. *Phys. Rev. B* **108**, 085437 (2023).
25. Boross, P. & Pályi, A. Braiding-based quantum control of a Majorana qubit built from quantum dots. *Phys. Rev. B* **109**, 125410 (2024).
26. Tsintzis, A., Souto, R. S., Flensberg, K., Danon, J. & Leijnse, M. Majorana qubits and non-abelian physics in quantum dot–based minimal Kitaev chains. *PRX Quantum* **5**, 010323 (2024).
27. Aasen, D. et al. Milestones toward Majorana-based quantum computing. *Phys. Rev. X* **6**, 031016 (2016).
28. Knapp, C. et al. The nature and correction of diabatic errors in anyon braiding. *Phys. Rev. X* **6**, 041003 (2016).
29. Nag, A. & Sau, J. D. Diabatic errors in Majorana braiding with bosonic bath. *Phys. Rev. B* **100**, 014511 (2019).
30. Bauer, B., Karzig, T., Mishmash, R. V., Antipov, A. E. & Alicea, J. Dynamics of Majorana-based qubits operated with an array of tunable gates. *SciPost Phys.* **5**, 4 (2018).
31. Karzig, T., Cole, W. S. & Pikulin, D. I. Quasiparticle poisoning of Majorana qubits. *Phys. Rev. Lett.* **126**, 057702 (2021).
32. Domínguez, F. & Yeyati, A. L. Quantum interference in a cooper pair splitter: the three sites model. *Physica E* **75**, 322–329 (2016).
33. Kiršanskas, G., Goldstein, M., Flensberg, K., Glazman, L. I. & Paaske, J. Yu-Shiba-Rusinov states in phase-biased superconductor–quantum dot–superconductor junctions. *Phys. Rev. B* **92**, 235422 (2015).
34. Grove-Rasmussen, K. et al. Yu–Shiba–Rusinov screening of spins in double quantum dots. *Nat. Commun.* **9**, 2376 (2018).
35. Luh, Y. Bound state in superconductors with paramagnetic impurities. *Acta Phys. Sin.* **21**, 75 (1965).
36. Shiba, H. Classical spins in superconductors. *Prog. Theor. Phys.* **40**, 435–451 (1968).
37. Rusinov, A. Theory of gapless superconductivity in alloys containing paramagnetic impurities. *Sov. Phys. JETP* **29**, 1101–1106 (1969).
38. Stanescu, T. D., Sau, J. D., Lutchyn, R. M. & Das Sarma, S. Proximity effect at the superconductor–topological insulator interface. *Phys. Rev. B* **81**, 241310 (2010).
39. Antipov, A. E. et al. Effects of gate-induced electric fields on semiconductor Majorana nanowires. *Phys. Rev. X* **8**, 031041 (2018).
40. Satori, K., Shiba, H., Sakai, O. & Shimizu, Y. Numerical renormalization group study of magnetic impurities in superconductors. *J. Phys. Soc. Jpn.* **61**, 3239–3254 (1992).
41. Bauer, J., Oguri, A. & Hewson, A. C. Spectral properties of locally correlated electrons in a bardeen–cooper–schrieffer superconductor. *J. Phys.* **19**, 486211 (2007).
42. Zitko, R., Bodensiek, O. & Pruschke, T. Effects of magnetic anisotropy on the subgap excitations induced by quantum impurities in a superconducting host. *Phys. Rev. B* **83**, 054512 (2011).
43. Hatter, N., Heinrich, B. W., Ruby, M., Pascual, J. I. & Franke, K. J. Magnetic anisotropy in shiba bound states across a quantum phase transition. *Nat. Commun.* **6**, 8988 (2015).
44. Yao, N. Y. et al. Phase diagram and excitations of a Shiba molecule. *Phys. Rev. B* **90**, 241108 (2014).

45. Scherübl, Z. et al. Large spatial extension of the zero-energy Yu–Shiba–Rusinov state in a magnetic field. *Nat. Commun.* **11**, 1834 (2020).
46. Scherübl, Z. et al. From cooper pair splitting to nonlocal spectroscopy of a Shiba state. *Phys. Rev. Res.* **4**, 023143 (2022).
47. Eldridge, J., Pala, M. G., Governale, M. & König, J. Superconducting proximity effect in interacting double-dot systems. *Phys. Rev. B* **82**, 184507 (2010).
48. Su, Z. et al. Andreev molecules in semiconductor nanowire double quantum dots. *Nat. Commun.* **8**, 585 (2017).
49. Scherübl, Z., Pályi, A. & Csonka, S. Transport signatures of an Andreev molecule in a quantum dot–superconductor–quantum dot setup. *Beilstein J. Nanotechnol.* **10**, 363–378 (2019).
50. Kürtössy, O. et al. Andreev molecule in parallel inas nanowires. *Nano Lett.* **21**, 7929–7937 (2021).
51. Danon, J. et al. Nonlocal conductance spectroscopy of Andreev bound states: symmetry relations and BCS charges. *Phys. Rev. Lett.* **124**, 036801 (2020).
52. Pan, H. & Das Sarma, S. Majorana nanowires, Kitaev chains, and spin models. *Phys. Rev. B* **107**, 035440 (2023).
53. ten Haaf, S. L. D. et al. A two-site Kitaev chain in a two-dimensional electron gas. *Nature* **630**, 329–334 (2024).
54. Zatelli, F. et al. Robust poor man's majorana zero modes using Yu-Shiba-Rusinov states. https://arxiv.org/abs/2311.03193 (2023).
55. Liu, C.-X. et al. Enhancing the excitation gap of a quantum-dot-based Kitaev chain (2023).

Acknowledgements

This work was supported by a subsidy for top consortia for knowledge and innovation (TKI toeslag), by the Dutch Organization for Scientific Research (NWO), by the European Union's Horizon 2020 research and innovation program FET-Open Grant No. 828948 (AndQC), and by Microsoft Corporation. AMB acknowledges NWO (HOTNANO) for the research funding.

Author contributions

C.-X.L. designed the project with input from F.Z., S.L.D.t.H., T.D., and M.W. C.-X.L., and A.M.B. performed the calculations and generated the figures. All authors contributed to the discussions and interpretations of the results. C.-X.L. and M.W. supervised the project. C.-X.L., A.M.B., and M.W. wrote the paper with input from F.Z., S.L.D.t.H., and T.D.

Competing interests

The authors declare no competing interests.

Additional information

Supplementary information The online version contains supplementary material available at https://doi.org/10.1038/s42005-024-01715-5.

Correspondence and requests for materials should be addressed to Chun-Xiao Liu.

Peer review information *Communications Physics* thanks the anonymous reviewers for their contribution to the peer review of this work. A peer review file is available.